21AM1A-05

Imaging of pedestrians with UWB Doppler radar interferometry

Kenshi Saho #1, Takuya Sakamoto #, Toru Sato #

Department of Communications and Computer Engineering, Kyoto University
Yoshida-Hommachi, Sakyo-ku, Kyoto, Japan
1 ksaho@sato-lab.0t0.jp

***Abstract*—This paper presents human imaging using ultra-wideband (UWB) Doppler radar. Our proposed method estimates three-dimensional human images using interferometry and, from velocity information, rejects false images created by the interference of body parts. Experiments show that our proposed method achieves high-resolution imaging of a variety of pedestrians in a realistic situation, and their motion features are confirmed with the estimated images.**

I. Introduction

Human imaging using radar has great potential for use in surveillance and monitoring systems in towns, houses, shops, and hospitals. A number of radar localization and imaging methods have been proposed and applied to detect human bodies [1]-[3]. However, most of these methods need large antenna arrays or many radars placed at various locations, therefore the size of the system and cost have increased. For human tracking with a small number of antennas, Lin and Ling [4], [5] proposed a continuous wave (CW) Doppler radar interferometric imaging method. However, this method generates many false images because of interference from multiple targets, and has insufficient resolution.

To resolve these problems, this study applies an Ultra Wide-Band (UWB) Doppler radar interferometric imaging method [6], [7] to human imaging. To reduce the occurrence of false images in the interferometry process, we introduced a false image detection and rejection method based on velocity information [7]. In this paper, we show experimentally that the proposed rejection method reduces false images, and realizes satisfactory human imaging. Moreover, applications in a realistic environment showed that our proposed method achieved high-resolution imaging of pedestrians moving in various directions and with various types of gait. In addition, their motion features were confirmed with the estimated images.

II. Proposed UWB Doppler Radar Imaging Method

A. System Configuration

Fig. 1 is a schematic of the setup for the UWB Doppler radar. We assumed that the target would be a pedestrian. Transmitting antenna Tx and receiving antennas Rx_1, $_2$, and $_3$ are set up in the $y = 0$ plane. The positions of antennas Tx, Rx_1, Rx_2, and Rx_3 are expressed as (x, z) = ($d/2$, $d/2$+z_c),(-$d/2$, -$d/2$+z_c), ($d/2$, -$d/2$+z_c), and (-$d/2$, $d/2$+z_c). The pair of receiving antennas Rx_1 and Rx_2 forms a horizontal interferometer and the pair of Rx_1 and Rx_3 forms a vertical interferometer. Measurements are conducted in various antenna positions and imaging results are acquired by superpositioning the results from each position z_c. The transmitting signal is a continuous wave (CW) signal with a frequency of f_0 modulated with an m-sequence of chip width t_C, which gives a range resolution of $\Delta R = ct_\mathrm{C}/2$ [8], [9], where c is the speed of light. The received signal waveform $s_{ik}(t)$ in range k using receiver i is acquired by taking a cross-correlation of raw received signals with a time-shifted m-sequence [8].

B. UWB Doppler Radar Interferometry

The UWB Doppler radar imager separates multiple scattering centers in the time-frequency distribution and estimates the positions of the extracted scattering centers using interferometry [6] [7]. If different scattering centers have different radial velocities, we can separate these using the differences in their Doppler frequencies. The Doppler frequency is expressed as:

$$f_\mathrm{d} = \frac{2v_\mathrm{d}}{\lambda}, \tag{1}$$

where v_d is the radial velocity and λ is the wavelength. The f_d for each instance in time is determined by time-frequency analysis of the received signals. The time-frequency distribution $S_{ik}(t, v_\mathrm{d})$ in this study was obtained by using a sliding-window discrete Fourier transform (SDFT) [10] of $s_{ik}(t)$. $S_{ik}(t, v_\mathrm{d})$ is calculated by:

$$S_{ik}(t, v_\mathrm{d}) = \int_{-\infty}^{\infty} s_{ik}(\tau) w_\mathrm{H}(\tau - t) \mathrm{e}^{-j4\pi v_\mathrm{d}\tau/\lambda} \mathrm{d}\tau, \tag{2}$$

where $j = \sqrt{-1}$ and $w_\mathrm{H}(t)$ is the Hamming window function. The SDFT calculates Eq.(2) for all the time bins. We extract significant peaks of $S_{ik}(t, v_\mathrm{d})$, which correspond to the scattering centers.

We then estimate the position of each extracted scattering center. The direction-of-arrival (DOA) is estimated by means of interferometry. Elevation DOA $\theta_{\mathrm{EL}n}$ and azimuth DOA $\theta_{\mathrm{AZ}n}$ of the n-th scattering center are calculated by:

$$\theta_\mathrm{EL}(t, v_{\mathrm{d}n}) = \sin^{-1}\left[\frac{\angle S_{1k'}(t, v_{\mathrm{d}n}) - \angle S_{3k'}(t, v_{\mathrm{d}n})}{(2\pi d/\lambda)}\right], \tag{3}$$

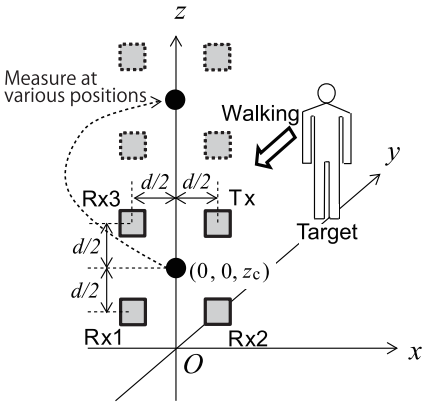

Fig. 1. Schematic of setup for UWB Doppler radar.

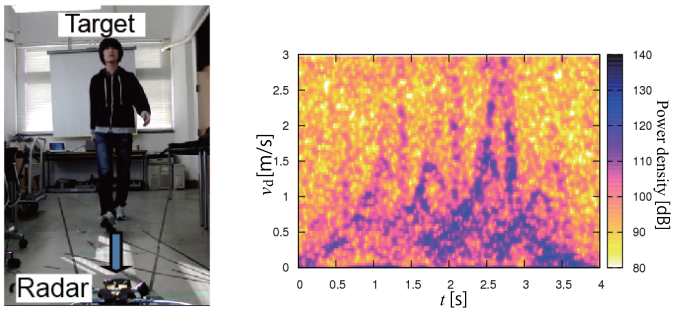

(a) Experimental site (b) Summation of the spectrograms for range bins

Fig. 2. Experimental setup and spectrogram at $z_{\rm c} = 0.36$ m of a pedestrian.

$$\theta_{\rm AZ}(t, v_{\rm dn}) = \sin^{-1}\left[\frac{\angle S_{1k'}(t, v_{\rm dn}) - \angle S_{2k'}(t, v_{\rm dn})}{\{2\pi d \cos\theta_{\rm EL}(t, v_{\rm dn})/\lambda)\}},\right], \quad (4)$$

where k' is the range bin where target n is detected. Distance $R(t, v_{\rm dn})$ is estimated by finding the range that maximizes the echo intensity with the method of range interpolation [6]. The positions of scattering centers $\mathbf{x}_{\rm s}(t, v_{\rm dn})$ are determined by:

$$\mathbf{x}_{\rm s}(t, v_{\rm dn}) = \begin{bmatrix} R(t, v_{\rm dn}) \cos\theta_{\rm EL}(t, v_{\rm dn}) \sin\theta_{\rm AZ}(t, v_{\rm dn}) \\ R(t, v_{\rm dn}) \cos\theta_{\rm EL}(t, v_{\rm dn}) \cos\theta_{\rm AZ}(t, v_{\rm dn}) \\ R(t, v_{\rm dn}) \sin\theta_{\rm EL}(t, v_{\rm dn}) + z_{\rm c} \end{bmatrix}. \quad (5)$$

C. False Image Rejection Method

The UWB Doppler radar interferometry described in the previous section, however, generates many false images. This is because this method assumes all scattering centers have different radial velocities. To resolve this problem, we proposed a false image detection and rejection method using velocity information [7]. The properties of this type of false image are [7]:

- Most false images have a relatively high apparent velocity because temporal phase continuity is not guaranteed for false images.
- Some false images are generated as an isolated point group.

Based on these, we remove the image that satisfies $v_{\rm max} < |\mathbf{v}(t, v_{\rm d})|$, where $\mathbf{v}(t, v_{\rm d}) = {\rm d}\mathbf{x}_{\rm s}(t, v_{\rm d})/{\rm d}t$ is the velocity of the estimated scattering center, and $v_{\rm max}$ is the assumed maximum speed. Next, we remove the isolated points. We assume a sphere with radius $R_{\rm F}$ whose center for each point is $\mathbf{x}_{\rm s}(t, v_{\rm d})$, and count the number of points $N_{\rm F}$ within this sphere. If $N_{\rm F}/N_{\rm A} < \alpha$, we rejecte these scattering centers, where $N_{\rm A}$ is the number of all estimated points and $\alpha(< 1)$ is empirically determined.

III. Imaging Examples for a Variety of Pedestrians in a Realistic Situation

A. Experimental Setup

In this section, examples of applications of the proposed UWB Doppler radar imaging method for various types of pedestrians are shown with experiments. The radar parameters were d=3.5 cm, f_0=26.4 GHz, and $t_{\rm C}$=2 ns, which corresponded to ΔR=30 cm. Horn antennas with $-$3dB beamwidth of $\pm$ 11° on both the E- and H-planes were used. We took measurements at four antenna positions for the acquisition of data that corresponded to the whole body: $z_{\rm c}$= 0.36, 0.83, 1.3, and 1.5 m. The interpulse period was 1.29 ms, and the window size for SDFT was 165 ms. The parameters for the false image rejection method were $v_{\rm max}$=2.5 m/s, $R_{\rm F} = \Delta R/10 = 3$ cm, and α=1/400.

B. Imaging of a Pedestrian Walking toward the Radar

In this subsection, we show the imaging example of a pedestrian target and the effectiveness of the proposed false image rejection method. The target walked from $(x, y) = (0, 3.9\ {\rm m})$ to $(0, 1.5\ {\rm m})$ with a step of 0.6 m and a mean speed of 0.86 m/s. The height of the examinee was 1.75 m. Figs. 2(a) and (b) show the experimental site and summation of the spectrograms for all range bins at $z_{\rm c} = 0.36$ m. The radial velocity variations of his legs were confirmed in the spectrogram, and the offset of the spectrogram corresponded to the mean walking speed.

Fig. 3 shows the frontal views of the image estimated using only the UWB Doppler radar interferometry (left panel) and the estimated image after applying the proposed false image rejection method (right panel). We can see that the proposed method rejects almost all the false images, and estimates scattering centers for each of the body parts. An outline of the human shape was accurately extracted. Fig. 4 shows the side view of the estimated image with the false image rejection method. In $z < 0.8$ m, the scattering centers with relatively large velocities correspond to the swinging leg, and the scattering centers with small $v_{\rm d}$ correspond to the leg in contact with the ground. Moreover, the swinging motion of the arm was detected as relatively large velocities over about 0.8 m $< z <$ 1.3 m. These results mean that we can confirm the walking motion features, and verify that the proposed imaging algorithm achieves adequate human imaging in a realistic environment.

C. Application to Pedestrians Moving in Various Directions

This subsection shows imaging examples of pedestrian targets moving in a variety of directions. First, we assumed

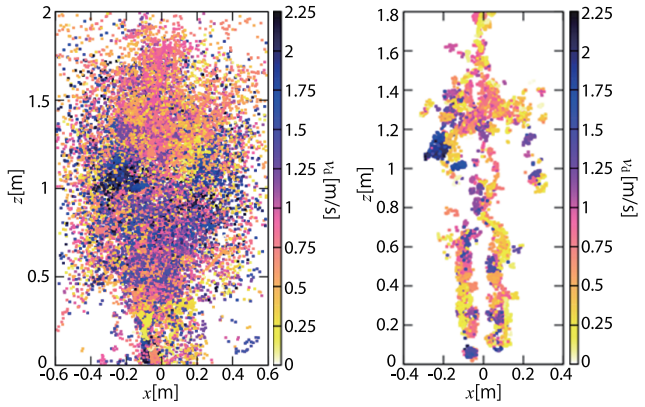

Fig. 3. Frontal views of the estimated image without (left) and with (right) the false image rejection method.

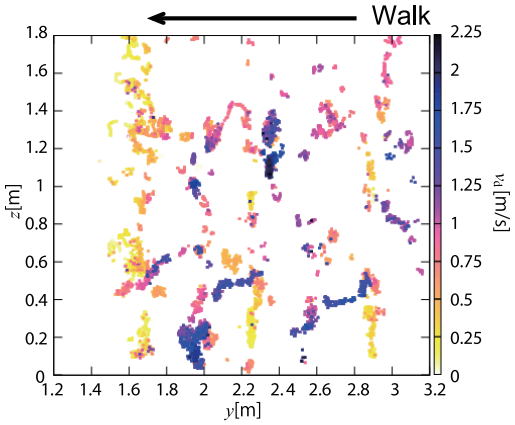

Fig. 4. Side views of the estimated image of a pedestrian walking toward the radar along the y-axis.

a pedestrian walking away from the radar. The target walked from (x, y)=(0 m, 1.5 m) to (0 m, 3.9 m) with a walking step of 0.6 m and a mean speed of 0.86 m/s. The height of the examinee was 1.63 m. Fig. 5 shows the frontal and side views of the estimated image using the data with a sufficient signal-to-noise ratio. This figure confirms that the human outline and features of walking motion were obtained as the example described in the previous section.

Next, we show the imaging results of pedestrians walking in oblique directions. We assumed two scenarios: case A assumed the target walks from (x, y)=(-1.03 m, 2.69 m) to (1.03 m, 1.51 m) and case B assumed the target walks from (x, y)=(-1.03 m, 2.41 m) to (1.03 m, 1.79 m). In both scenarios, the mean speed and the height of the target were 0.8 m/s and 1.78 m. Fig. 6 shows the top and frontal views of the estimated image for case A, where X is the axis perpendicular to the walking direction. We used the data that correspond to the target within the illumination area of the beam. Although there was a small number of scattering centers in the relatively large X because of shadowing, a human outline and walking orbit were correctly detected. Fig. 7 shows the top and frontal views of the estimated image for case B. The radial velocities became

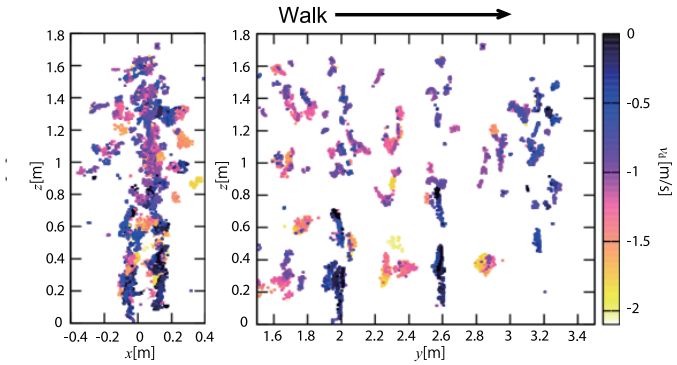

Fig. 5. Frontal (left) and side views (right) of the estimated image of a pedestrian walking away from the radar along the y-axis.

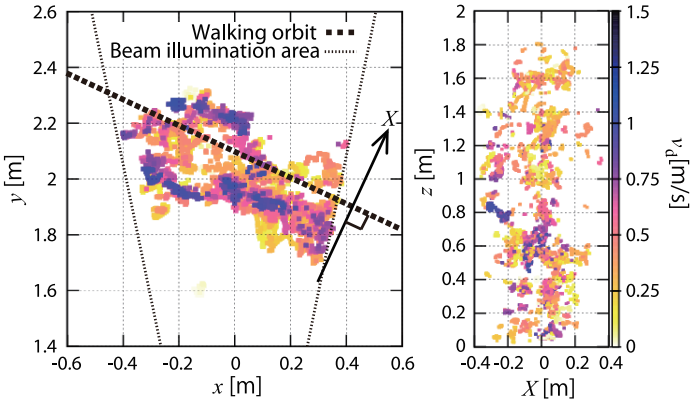

Fig. 6. Top (left) and frontal views (right) of the estimated image of a pedestrian walking in an oblique direction (case A).

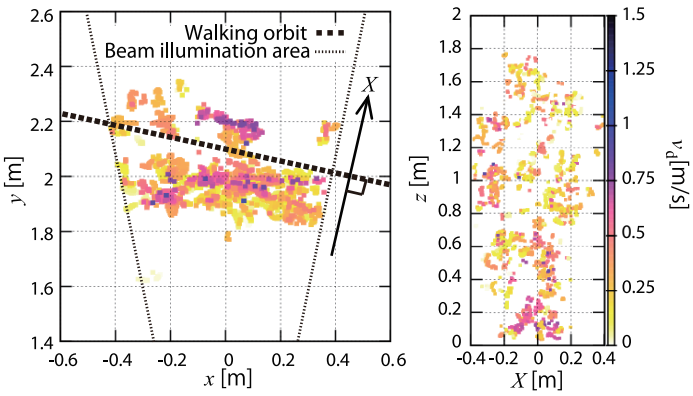

Fig. 7. Top (left) and frontal views (right) of the estimated image of a pedestrian walking in an oblique direction (case B).

small compared with case A because the walking orbit was close to the cross-range direction. In addition, the effect of shadowing was larger than in case A. However, the walking orbit and the human outline were extracted to some extent. These results indicate that our proposed method is applicable to target motion with arbitrary directions.

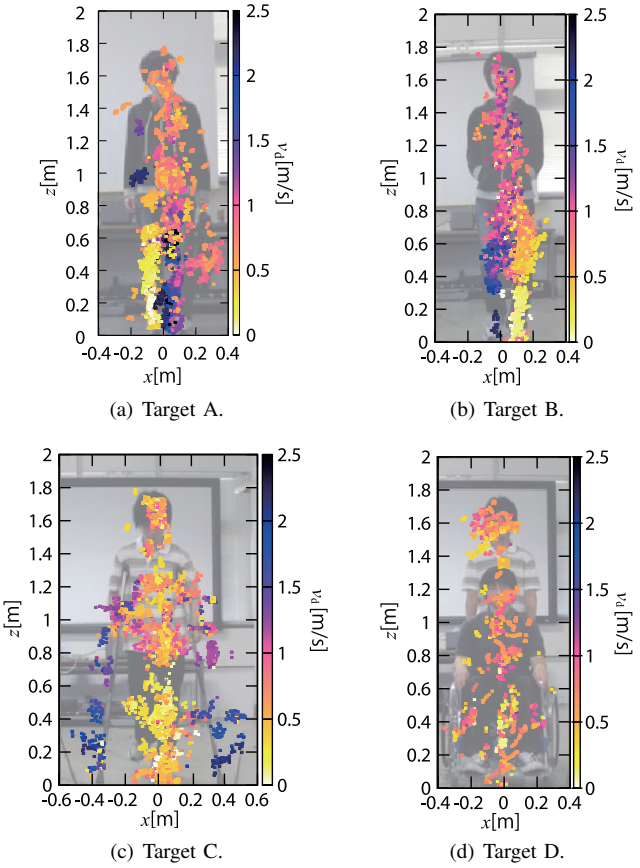

(a) Target A. (b) Target B. (c) Target C. (d) Target D.

Fig. 8. Frontal views of the estimated images of various pedestrian targets.

D. Application to Various Types of Pedestrians

This section presents imaging examples of various types of pedestrians, and discusses the features of each image. We assumed four types of pedestrians: target A carried a bag in his left hand, target B walked with his hands in his pockets, target C was a pedestrian with a three-point crutch swinging gait, and target D was a pedestrian pushing a person in a wheelchair. All targets walked from (x, y) =(0, 3.9 m) to (0, 1.5 m). The mean speeds of targets A, B, C and D were 0.8, 0.8, 0.76 and 0.7 m/s, and they walked at an approximately constant speed. We used data corresponding to one cycle of a time-frequency distribution for imaging.

Fig. 8 shows the frontal views of the estimated images for all pedestrian types. As we can see from Fig. 8(a), there is an outline of the human shape in the frontal view of the estimated images of target A. Moreover, we can recognize from radial velocity information that the left leg and the right arm have forward motion in this half of the walking cycle, and can observe the scattering centers on the bag at approximately (x, z) =(0.25 m, 0.5 m). Fig. 8(b) indicates that scattering centers corresponding to the arms have not been acquired. This is because the peaks corresponding to the arms were not detected in the time-frequency distribution because there was no arm motion for target B. We can confirm the images of crutches and their relatively high velocities that correspond to their forward motion as seen in Fig. 8(c). Fig. 8(d) shows the scattering centers are concentrated in a relatively narrow region in terms of both the position and v_{d}. This is because target D was moving toward the radar at an approximately constant velocity. These results indicate that the method of UWB Doppler radar imaging can accurately represent a variety of pedestrians, and the features of each pedestrian can be confirmed from the radial velocity information of the estimated images.

IV. Conclusions

This paper presented the imaging of pedestrians using UWB Doppler radar in a realistic situation. We explained the operation of UWB Doppler radar interferometry for obtaining human images, and applied the false image rejection method using velocity information. The experiment, which assumed a variety of pedestrians, showed that the proposed imaging algorithm achieved adequate imaging and the motion features of various pedestrians were confirmed with the estimated images.

Acknowledgments

The authors sincerely thank Messrs. Takeshi Fukuda and Kenichi Inoue of the Panasonic Corporation for their valuable comments and significant support with radar hardware.

References

[1] A. Dhital, P. Closas and C. Fernández-Prades, "Bayesian filtering for indoor localization and tracking in wireless sensor networks," *EURASIP J. Wirel. Commun. Netw.*, Article Number 21, 2012.

[2] S. Hantscher, B. Schlenther, M. Hagelen, S.A. Lang, H. Essen, A. Tessmann, A. Hulsmann, A. Leuther and M. Schlechtweg, "Security prescreening of moving persons using a rotating multichannel W-Band radar," *IEEE Trans. Micro. Theo. Tech.*, vol. 60, no. 3, pp. 870–880, 2012.

[3] Y. Wang and A.E. Fathy, "Advanced system level simulation platform for three-dimensional UWB through-wall imaging SAR using time-domain approach," *IEEE Trans Geosci. Remote Sens.*, vol. 50, No. 5, pp. 1986–2000, 2012.

[4] A. Lin and H. Ling, "Doppler and direction-of-arrival (DDOA) radar for multiple-mover sensing," *IEEE Trans. Aero. Elec. Sys.*, vol. 43, no. 4, pp. 1496–1509, 2007.

[5] A. Lin and H. Ling, "Frontal imaging of human using three element Doppler and direction-of-arrival radar," *Electronics Letters*, vol. 42, no. 11, pp. 660–661, 2006.

[6] K. Saho, T. Sakamoto, T. Sato, K. Inoue and T. Fukuda, "High-resolution UWB Doppler radar interferometric imaging algorithm for multiple moving targets with smoothed pseudo Wigner distribution," *IEICE Tech. Rep.*, vol. 110, no. 250, pp. 261–266, 2010.

[7] K. Saho, T. Sakamoto, T. Sato, K. Inoue and T. Fukuda, "Experimental study of real-time human imaging using UWB Doppler radar interferometry," *Proc. 6th European Conf. Antennas and Propagation (EuCAP2012)*, Prague, Chech Republic, M16-3, 2012.

[8] R. Pickholts, D. Schilling and L. B. Milstein, "Theory of Spread-Spectrum Communications-A Tutorial," *IEEE Trans. Commun.*, vol. COM–30, pp. 855–882, 1982.

[9] T. Fukuda, N. Nagoro, S. Ujita, S. Nagai, M. Nishijima, H. Sakai, T. Tanaka and D. Ueda, "A 26GHz short-range UWB vehicular radar using 2.5 Gcps spread spectrum modulation," *Microwave Symposium, 2007. IEEE/MTT-S International*, pp. 1311-1314, 2007.

[10] E. Jacobsen and R. Lyons, "The Sliding DFT," *IEEE Trans. Sig. Proc. Mag.*, vol. 20, no. 2, pp. 74–80, 2003.